Centroid-Predicted Deep Neural Network in Shack-Hartmann Sensors

Mengmeng Zhao, Wang Zhao, Shuai Wang, Ping Yang, Kangjian Yang, Haiqi Lin, and Lingxi Kong

***Abstract*—The Shack-Hartmann wavefront sensor produces incorrect wavefront measurements when some sub-spots are weak and missing. In this paper, a method is proposed to predict the centroids of these sub-spots for the Shack-Hartmann wavefront sensor based on the deep neural network. Using the centroid information of present sub-spots, the method is able to predict the absent sub-spots' positions. The feasibility and effectiveness of this method are verified by a large number of numerical simulations. The method is applied to wavefront measurement of light with non-uniform near-field intensity. The simulation results show that the proposed method is of great help to improve the measurement accuracy and the Strehl ratio of the focal spot. For wavefronts outside of the training sample, the proposed method shows good generalization and adaptability. In addition, the experiment results demonstrate that the proposed method can predict the missing sub-spots' centroid displacements accurately even though a large proportion of sub-spot is lost randomly.**

***Index Terms*—Centroid prediction, deep neural network, Shack-Hartmann sensors, missing sub-spots, low signal-to-noise ratio.**

I. Introduction

THE Shack-Hartmann wavefront sensor (SHWFS) has been widely used in astronomy [1], biological imaging [2], [3], ophthalmology [4], [5], and laser beam characterization [6], [7]. The SHWFS provides the measurement of the slopes of the wavefront by calculating the centroid displacements of each sub-spot [8]. The incident wavefront is then reconstructed from the slopes by wavefront reconstruction algorithms [9–12]. Therefore, the accuracy of centroid calculation determines the wavefront reconstruction precision of a SHWFS. For a conventional SHWFS, each subaperture has a corresponding sub-spot whose centroid displacements represent the local slop information. However, traditional centroid calculation methods [13]-[15], calculating the average positions of the intensity distribution in a specified region within the subaperture, are invalid because of the absence of spots caused by scintillation, extended propagation paths, cloud obscuration, and non-uniform illumination [16]–[18]. Moreover, the position and number of missing sub-spots are random and dynamic [19]. These random undetected local slop values will cause an unstable and inaccurate wavefront measurement.

To improve the accuracy of the SHWFS with missing some sub-spots, researchers have proposed several methods. Some have focused on reducing the number of subapertures to avoid the absence of sub-spots [20]-[22], but these methods change the structure of the SHWFS and increase the complexity of the system. Thus, a method is needed to recover the information of missing sub-spots to improve the measurement precision of the SHWFS. Recently, the application of machine learning to Shack-Hartmann wavefront sensing technology has become a research hotspot. Guo *et al.* predict low-order Zernike coefficients from the x and y spot displacements based on the back-propagation (BP) neural network [23]. Li *et al.* apply the artificial neural network (ANN) to centroid computation for a SHWFS in some extreme situations [24]. Hu *et al.* propose a convolutional neural network (CNN) to directly predict the Zernike coefficients from the output pattern of the SHWFS, in order to improve the measurement precision of the SHWFS for the high-order aberration [25]. Swanson *et al.* use a U-net and long-short term memory (LSTM) network to predict the wavefront based on x and y slopes [26]. Du Bose *et al.* present an intensity/slopes network (ISNet) to reconstruct the wavefront with both the wavefront slopes and the intensity of subapertures, improving the wavefront reconstruction accuracy in the presence of non-uniform illumination [27]. Hu *et al.* apply a modified U-net network to directly reconstruct the wavefront distribution from the pattern of the SHWFS with a lower root mean square (RMS) wavefront error [28]. All the above methods demonstrate that machine learning can improve the performance of the SHWFS. However, these methods are performed when each subaperture can detect the optical signal. They depend on the complete output pattern of the SHWFS.

In terms of missing spots due to the near-field non-uniformity of the beam and the limited dynamic range of the camera, a deep learning-based approach is provided in this paper. We are no longer concerned with wavefront prediction as studied above. Instead, we first treat the inaccurately detectable spots as missing

Manuscript received September 12, 2021; revised October 22, 2021; accepted October 25, 2021. Date of publication October 29, 2021; date of current version December 20, 2021. This work was supported in part by National Natural Science Foundation of China under Grant 61805251, 61875203 and 11704382, in part by Youth Innovation Promotion Association CAS under Grant 2017429, in part by Western Youth Scholar A CAS, and in part by CAS "Light of West China" Program. *(Corresponding author: Shuai Wang.)*

Mengmeng Zhao and Lingxi Kong are with the Key Laboratory on Adaptive Optics, Chinese Academy of Sciences, Chengdu, Sichuan 610209, China, with the Institute of Optics and Electronics, Chinese Academy of Sciences, Chengdu, Sichuan 610209, China, and also with the University of Chinese Academy of Sciences, Beijing 100049, China (e-mail: zhaomengmeng18@mails.ucas.ac.cn; konglingxi18@mails.ucas.ac.cn).

Wang Zhao, Shuai Wang, Ping Yang, Kangjian Yang, and Haiqi Lin are with the Key Laboratory on Adaptive Optics, Chinese Academy of Sciences, Chengdu, Sichuan 610209, China, and also with the Institute of Optics and Electronics, Chinese Academy of Sciences, Chengdu, Sichuan 610209, China (e-mail: zw_2017@foxmail.com; wangshuai@ioe.ac.cn; pingyang2516@163.com; yangkangjian@ioe.ac.cn; tjlinhaiqi@163.com).

Digital Object Identifier 10.1109/JPHOT.2021.3123656

spots and then work on retrieving their information through the machine learning to improve the measurement precision of the SHWFS. We use a deep neural network to predict the missing sub-spots' position from the centroid-displacement information of detected sub-spots. This method enables the SHWFS more tolerant to the absence of some sub-spots. Besides, the method does not require changing the hardware architecture of the SHWFS and is compatible with conventional wavefront reconstruction algorithms.

The remaining part of the paper is organized as follows: Section II.A introduces the measurement principle of the SHWFS and the measurement error introduced due to the absence of sub-spots, Section II.B describes the structure of the constructed deep neural network, and Section II.C introduces the method of generating datasets; In Section III, the numerical simulation results are displayed to demonstrate the feasibility of the proposed model. Then, the experimental results are given in Section IV. Finally, we conclude the paper in Section V.

II. Methods

A. Shack-Hartmann Wavefront Sensor

A SHWFS consists of a microlens array and a detector located at the focal plane of the microlens array. It samples the incident wavefront through a microlens array, each of which creates a sub-spot on the camera. According to geometric optics, there is a linear relationship between the centroid displacements of each sub-spot and the average *x* and *y* slope of the wavefront, as described in Equation (1) [29]. Finally, the incident wavefront is reconstructed from average slopes.

$$\frac{\partial \phi}{\partial x}(x_i, y_i) \simeq \frac{\Delta x_i}{L} = \frac{x_i{}' - x_i}{L}$$
$$\frac{\partial \phi}{\partial y}(x_i, y_i) \simeq \frac{\Delta y_i}{L} = \frac{y_i{}' - y_i}{L} \tag{1}$$

Where ϕ is the wavefront function, Δx_i and $\Delta y_i$are the measured centroid displacements along the *x* and *y* directions of the sub-spot of the *ith* subaperture. *L* is the distance between the microlens array and detector, (x_i, y_i) is the *ith* sub-spot's centroid position corresponding to the plane wavefront, $(x_i{}', y_i{}')$ is the *ith* sub-spot's centroid position corresponding to the aberration wavefront.

The current common calculation methods for centroid position are the threshold center of gravity algorithms (*TCoG*), sunch as *TmCoG* (using m% of maximum intensity of sub-spot as the threshold) [14] and *TkCoG* (using $\mu_N + k\delta_N$ as the threshold, μ_N and $\delta_N$are the mean and standard deviation of the noise) [30]. It is able to reduce the effect of noise, and it can be written as:

$$x_i = \frac{\sum_{m=1}^{M}\sum_{n=1}^{N} x_{mn}(I_{mn} - T)}{\sum_{m=1}^{M}\sum_{n=1}^{N}(I_{mn} - T)};$$
$$y_i = \frac{\sum_{m=1}^{M}\sum_{n=1}^{N} y_{mn}(I_{mn} - T)}{\sum_{m=1}^{M}\sum_{n=1}^{N}(I_{mn} - T)} \tag{2}$$

Where (x_i, y_i) is the centroid of the *ith* sub-spot, (x_{mn}, y_{mn}) is the coordinate of pixel, I_{mn} is the corresponding intensity and *T* is the threshold value for splitting the signal and noise in the subaperture. However, when the subapertures' optical signal is weak or even annihilated in the noise,

$$\sum_{m=1}^{M}\sum_{n=1}^{N}(I_{mn} - T) \approx 0 \tag{3}$$

In this case, the centroid calculated by formula (2) will have anomalous values, leading to invalid wavefront reconstruction. To avoid this, the conventional method sets centroid displacements of the sub-spots to zero. But, as the number of such subapertures increases, the wavefront reconstruction error increases. Therefore, information on these subapertures needs to be processed in a timely manner.

In this paper, a method is proposed to process information on the subapertures with spot missing in real time. The method is based on the assumption that the wavefront is continuous and fits the response of the continuity on the centroid displacement using a deep neural network. The missing information is retrieved from the surrounding subapertures' information based on a well-trained deep neural network.

B. SH-U-Net Model

As shown in Fig. 1, the most typical U-Net structure [31] is used to design the deep neural network to predict the centroid displacements of missing sub-spots. We call the architecture the SH-U-Net model. The input of the SH-U-Net model is a 16×16×2 local *x* and *y* centroid-displacement matrix, as shown in Fig. 1(a), where the centroid displacements of the missing sub-spots are set to zero. It is first encoded 4 times in succession by the encoder, which consists of two 3 × 3 convolutional layers, each followed by a rectified linear unit (ReLu), and a 2 × 2 maximum pooling layer for performing down-sampling. Its depth features are finally encoded in a matrix of 2 × 2 × 512. It is then successively decoded by the decoder to recover the lateral size of 16 × 16. The decoder consists of a 2×2 up-convolutional layer for up-sampling and extending the depth features, a ReLU, and two 3×3 convolutional layers, each followed by a ReLU. Finally, the 16×16×2 global *x* and *y* centroid-displacement matrix is output by 1×1×2 convolutional layer and regression function, as shown Fig. 1(b). The centroid displacements of those missing sub-spots are predicted. The network also uses a skip connection to connect the output of each decoding block to the up-sampling result. The problem of gradient vanishing is solved by the skip-connection and the feature transfer is also enhanced. Finally, the centroids of the missing sub-spots are determined from the centroid displacements predicted by the SH-U-Net model.

C. Data Generation and Network Training

We first simulate 10000 sets of incident wavefronts characterized by the linear combination of the first 35 Zernike polynomials (excluding piston and tilt). The Zernike coefficients are generated randomly based on the Kolmogorov turbulence model [32].The ranges of turbulence model parameter D/r_0 are set from 5 to 10 (*D* is the effective aperture of the SHWFS, and r_0 is the

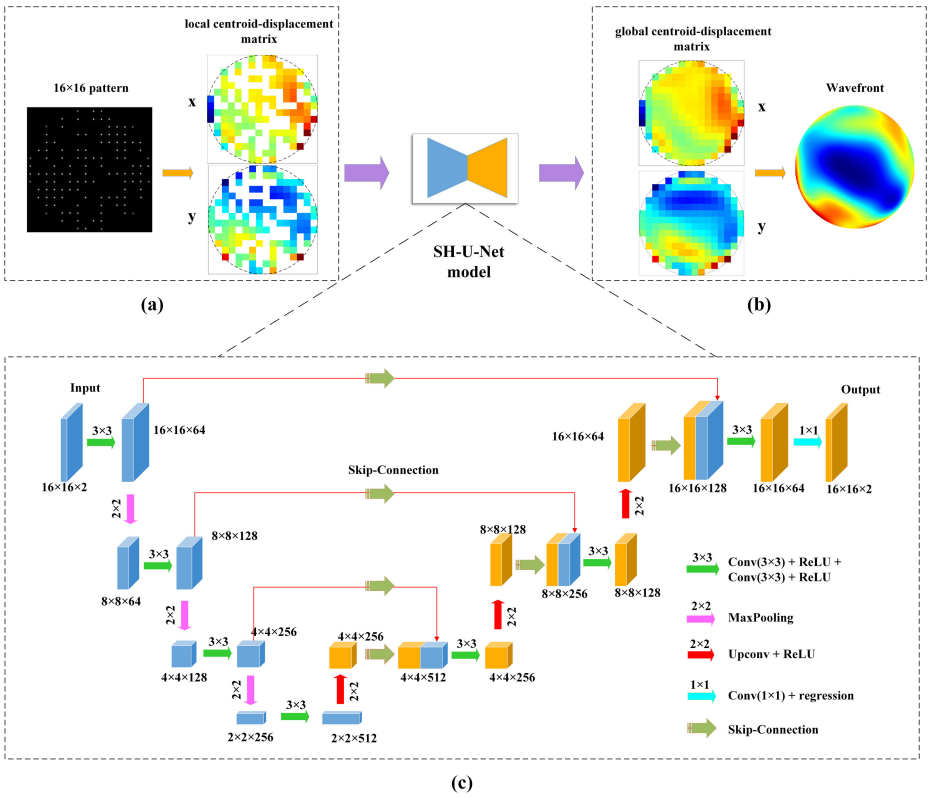

Fig. 1. Schematic diagram of the proposed method for centroid displacement prediction. (a) The input of the SH-U-Net model. (b) The output of the SH-U-Net model. (c) The architecture of the SH-U-Net model.

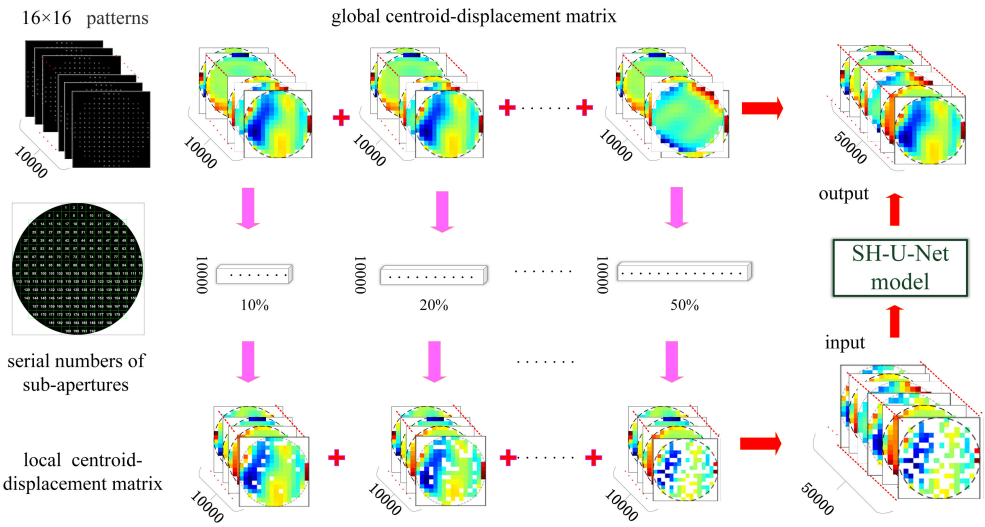

Fig. 2. The process of generating samples.

coherence length of the atmosphere). A 16 ×16 microlens array with 192 valid subapertures is used to sufficiently sample the incident wavefronts [33]. The key parameters of the SHWFS are list in Table. I. We input each wavefront into the Shack-Hartmann wavefront sensing system to generate the corresponding pattern, respectively.

Furthermore, photon noise and detector readout noise are also added to the patterns of the SHWFS in order to enhance the robustness of the network. In order to effectively reduce the interference of noise, we use the *TmCoG* algorithm to calculate the centroids of sub-spots and obtain the global centroid-displacement matrix. The process of generating samples is shown in Fig. 2. The 16×16×2 global centroid-displacement matrix is used as the output of the SH-U-Net model. To simulate the loss of N sub-spots, we rank the valid subapertures and create 1000 non-repeating sequences of N subapertures. The x and y

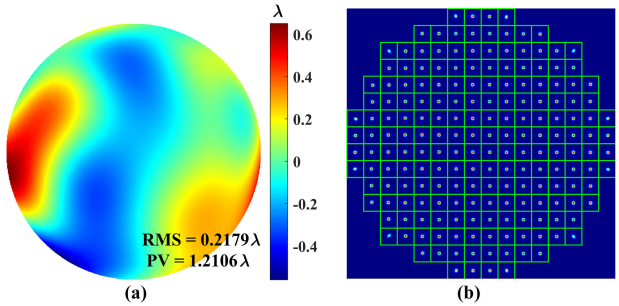

Fig. 3. Random incident wavefront. (a) The distribution of incident wavefront. (b) The output pattern of the SHWFS.

centroid displacements of the corresponding N sub-spots are set to zero, producing a local centroid-displacement matrix as input to the SH-U-Net model. This process is repeated to expand and enrich the training samples, and the number of missing sub-spots (*N*) is set to 10%, 20%, 30%, 40%, and 50% of the total sub-spots' number. Finally, 50000 sets of training samples are generated, and these samples are rearranged at random.

The entire training process of the network is performed on a desktop workstation (An Intel(R) Core (TM) i9 9900X (3.5 GHz), RAM (64 GB, 1600 MHz), NVIDIA GeForce GTX 1080Ti, with Windows10 operating system). To optimize the weights of the network, we use an adaptive moment estimation (Adam) optimizer with an initial learning rate of 0.001. During the training, the epoch is set to 200, the batch size is set to 128. The root mean square (RMS) of centroid displacement error between the predicted value and ground truth is used as the loss function.

$$RMS = \sqrt{\frac{\sum_{i=1}^{2M} (C_i - T_i)^2}{2M}} \tag{4}$$

where M represents the number of all sub-spots, $C_i$and $T_i$represent the forecasted and true values of centroid displacement for the *ith* subaperture. Since each spot's centroid displacement contains both x and y directions, a total of $2M$ values are predicted.

III. Simulations

A. Validation

To validate the feasibility and effectiveness of the SH-U-Net model, a series of numerical simulations under various conditions are conducted. Fig. 3 shows one typical group of incident wavefront and the corresponding complete output pattern of the SHWFS. This group is selected to validate the prediction accuracy of the SH-U-Net model.

By means of effective centroid displacement prediction, the wavefront can be reconstructed more accurately. The reconstructed wavefronts and residual wavefronts with the modal algorithm in different scenarios of the sub-spot missing are shown in Fig. 4. In the ideal scenario (no sub-spot missing), the RMS of the residual wavefront is 0.0018λ. As the number of missing sub-spots increases, the RMS of the residual wavefront of the non-predicted method keeps increasing. When 30% of total sub-spots are missing, the RMS of the residual wavefront rises to 0.0634λ, which means that the wavefront reconstruction precision of the SHWFS decreases by 28.36% and the wavefront cannot be reconstructed effectively. Compared with the non-predicted method, the SH-U-Net model significantly improves the wavefront reconstruction precision of the SHWFS benefit from the centroid displacement prediction. With 30% of total sub-spots missing, the SH-U-Net model provides the RMS of the residual wavefront of 0.0029λ, which is only 0.0011λ different from the ideal scenario.

To further investigate the generalization of the SH-U-Net model, we randomly generate 1000 sets of incident wavefronts and obtain 5000 sets of test samples by the method described in Section II.C. The number and locations of missing sub-spots are random. Fig. 5(a) shows the statistical results of the RMS of centroid-displacement prediction error in different scenarios. They are all kept below 1 pixels, indicating that the SH-U-Net model achieves the sub-pixel-level prediction for the centroids of the missing sub-spots.

We reconstruct the incident wavefronts using the modal algorithm for different scenarios. As shown in Fig. 5(b), with the number of the missing sub-spot increasing, the RMS of the residual wavefronts of the non-predicted method increases linearly, while that of the SH-U-Net model remains level with ideal scenario. The average RMS of the residual wavefronts is 0.0118λ in the ideal scenario. With 40% of total sub-spots missing, the average RMS of the residual wavefronts of the SH-U-Net model is 0.0128λ, which has 0.0010λ difference from the ideal scenario. Compared with the non-predicted method, the RMS of the residual wavefronts of the SH-U-Net model is reduced by 88.95%. These results show that the SH-U-Net model can accurately predict centroid displacements of missing sub-spots which is of great help to improve the measurement precision of the SHWFS.

B. Validation on Non-Uniform-Intensity Light

To investigate the reliability of the model, we create a simulation for a propagating beam of light through atmospheric turbulence. We explore propagation over a 1.84km with turbulence strength level (C_n^2) of 2.1×10^{-14} $m^{-2/3}$ and corresponding Rytov number (the log-amplitude variance of scintillation) of 0.2. We extract irrotational phase component[34], also known as the continuous phase, as our incident wavefront. Fig. 6 illustrates the amplitude, continuous phase distribution and the corresponding output pattern of the SHWFS for a beam of light. As shown in Fig. 6(a) and (b), the amplitude aberrations and phase aberrations are produced when the beam reaches the ground due to the atmospheric turbulence. This result causes the intensity of some imaged sub-spots to be diminished, and the sub-spots are even annihilated in the noise, as presented in Fig. 6(c). The added noise in the Fig. 6(c) follows a Gaussian distribution with a mean of 48 and a variance of 10. To express the quality of the spot in each subaperture, the peak signal-to-noise ratio (*SNRp*) was chosen as a measure [24].

$$SNR_p = \frac{I_p}{\delta_n} \tag{5}$$

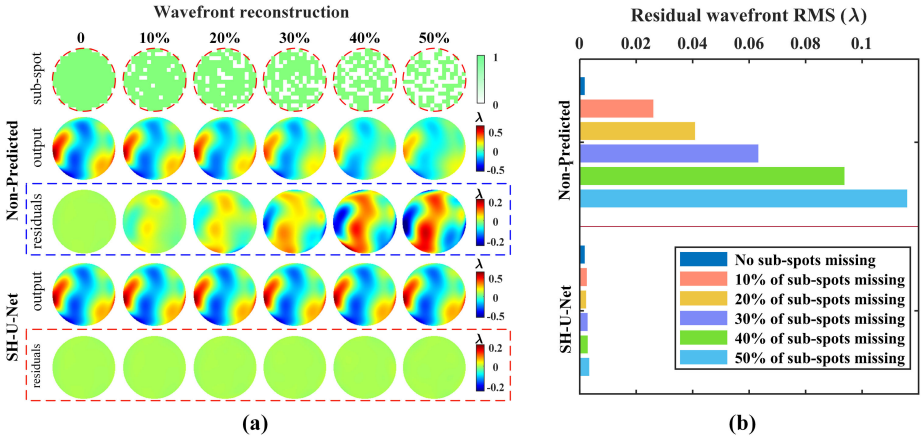

Fig. 4. The results of wavefront reconstruction for different scenarios of sub-spot missing. (a) The location of subapertures with missing spot, reconstructed wavefront, and residual wavefront for non-predicted and predicted methods. Here, 1 in the sub-spot means that there is sub-spot, and 0 means that the sub-spot is missing. (b) The RMS of residual wavefront for non-predicted and predicted methods.

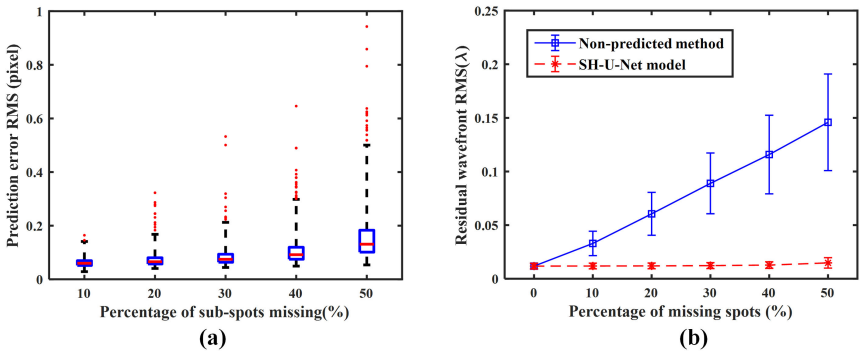

Fig. 5. The statistical results of the centroid displacement prediction and wavefront reconstruction for different scenarios. Each scenario contains 1000 datasets. (a) The RMS of centroid-displacement prediction errors. (b) The RMS of the residual wavefronts.

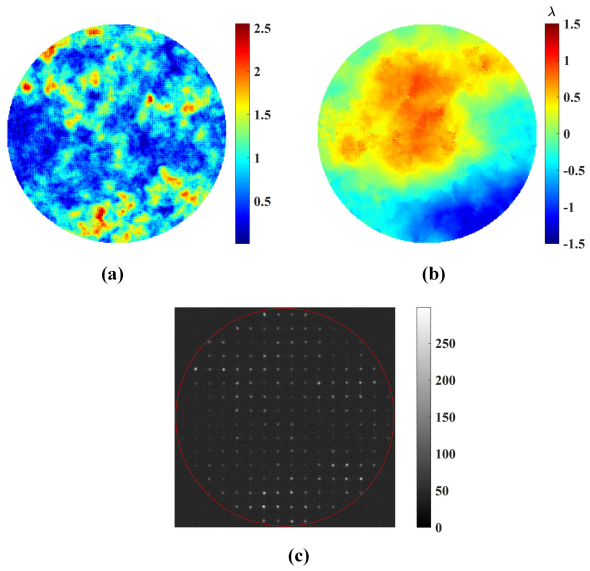

Fig. 6. (a) The amplitude distribution of the beam. (b) The phase distribution of the beam. (c) The output pattern of the SHWFS.

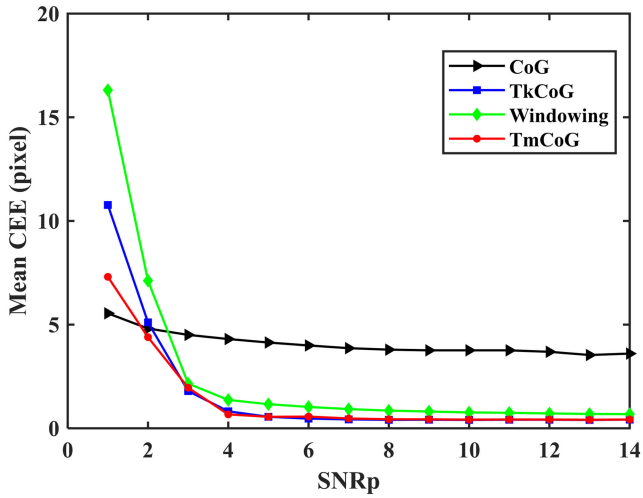

Fig. 7. CEE of different methods with different *SNRp*.

where $I_p$is the peak value of the sub-spots, and is $\delta_n$the standard deviation of the noise in the subaperture.

Effective predictions of the SH-U-Net model should be premised on accurate inputs. To be sure that the input data of the SH-U-Net model are reliable, we generated 1000 sets of output pattern of the SHWFS and calculated the centroids for each sub-aperture using the conventional centroid calculation methods, including the center of gravity (*CoG*) algorithm, the windowing algorithm, *TkCoG* algorithm *and TmCoG* algorithm[24]. We then compared the average centroid estimation error (CEE) [24]

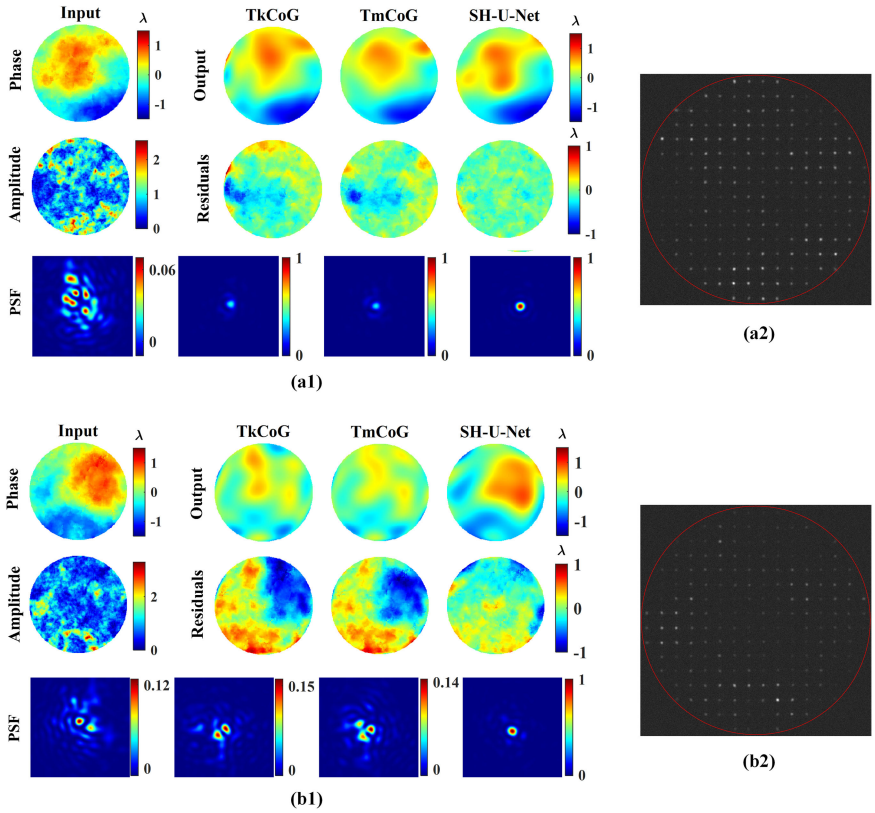

Fig. 8. Comparison of wavefront detection results of the two sets of test data for the three approaches. (a1) and (b1) Simulated turbulence phase screen, near-field amplitude distribution, reconstructed wavefront, residual wavefront, and corresponding point spread function (PSF) of test sample 1 and 2, respectively. (a2) and (b2) The output patterns of the SHWFS corresponding to test sample 1 and 2, respectively.

TABLE I
KEY PARAMETERS OF THE SHWFS

Parameters	value
wavelength(λ)	635 nm
microlens size	400μm
microlens numbers	16×16
focal length of the microlens	42.3mm
valid subaperture numbers	192
pixel size	6.4μm×6.4μm

of different methods with different *SNRp*, as shown in Fig. 7.

$$CEE = \sqrt{(x_c - x)^2 + (y_c - y)^2} \tag{6}$$

where (x,y) is the true centroid position, (x_c, y_c) is the calculated centroid position.

From Fig. 7, it is easy to see that the centroid positions cannot be calculated accurately in the case of the *SNRp* below 4. Compared to the other two methods, the CEE of *TmCoG* and *TkCoG* algorithms lower when *SNRp* is higher than 4. Therefore, we choose the *TmCoG* algorithm as the input basis for the SH-U-Net model, and set the centroid displacements of these sub-spots with *SNRp* below 4 to zero. Then, they are predicted by the SH-U-Net model.

Fig. 8 and Table II show the comparison results of the two sets of test data for three methods, which intuitively illustrate the characteristics of each method. Here, the wavefront reconstruction algorithms all use the modal algorithm. Fig. 8 (a2) and 8(b2) are the patterns of the SHWFS corresponding to test samples 1 and 2, respectively. The numbers of subapertures with *SNRp* below 4 are 62 and 117, approximately 32% and 61% of the effective numbers, respectively. The phase screen, near-field amplitude distribution, reconstructed wavefront, residual wavefront, and corresponding point spread function (PSF) for test samples 1 and 2 are presented in Fig. 8 (a1) and Fig. 8 (b1), respectively. The RMS of residual wavefront of the *TkCoG*, *TmCoG*, and SH-U-Net model in Fig. 8(a) are 0.2011λ, 0.1768λ, and 0.0942λ, respectively. The SH-U-Net model is able to achieve approximately 53.16% (*TkCoG*) and 46.72% (*TmCoG*) reduction in RMS of the residual wavefront, respectively. The Strehl ratio (SR) of corrected PSFs are 0.4152, 0.3753, and 0.7156, respectively. Our method improves SR of corrected PSFs by factors of 0.7235 (*TkCoG*) and 0.9058 (*TmCoG*), respectively.

The residual wavefront RMS in Fig. 8 (b1) are 0.4177λ (*TkCoG*), 0.3819λ (*TmCoG*), and 0.2143λ (SH-U-Net model), respectively. And the SR of corrected PSFs are 0.1613, 0.1440, and 0.4790, respectively. It is worth noting that the *TkCoG* and *TmCoG* approaches no longer accurately detect the wavefront aberration and the focal spots are dispersed. However, since the SH-U-Net model predicts the position of the sub-spots with low signal-to-noise ratio, the wavefront aberration can be effectively measured and the intensity of the focal spot in the concentrated area is substantially increased even though a large amount of subaperture information cannot be accurately detected.

TABLE II
THE PERFORMANCE OF THE FOUR METHODS

	PV/λ		RMS/λ		SR	
Test sample	Sample 1	Sample 2	Sample 1	Sample 2	Sample 1	Sample 2
Phase screen	2.3240	2.5288	0.5146	0.5355	0.0683	0.1274
TKCoG	1.9972	2.1225	0.2011	0.4177	0.4152	0.1613
TmCoG	1.3331	2.2089	0.1768	0.3819	0.3753	0.1440
SH-U-Net model	1.1770	1.654	0.0942	0.2143	0.7156	0.4790

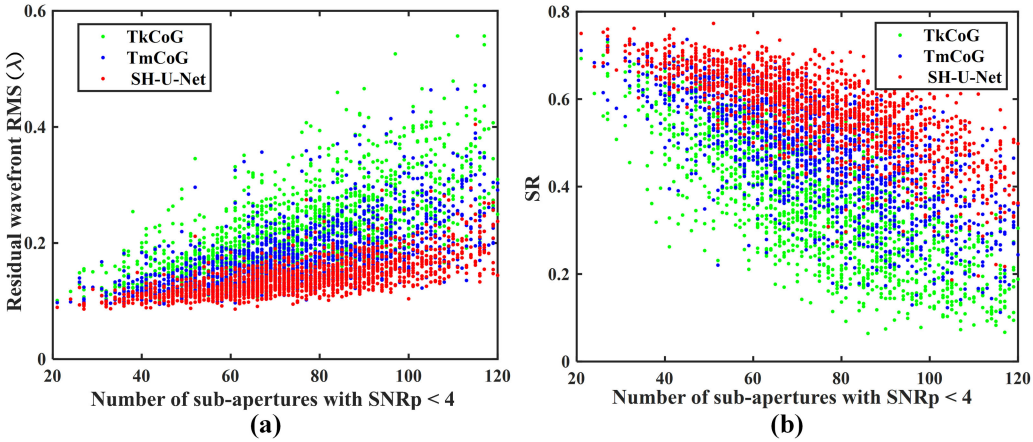

Fig. 9. Wavefront detection results of 1500 wavefronts for the three approaches. (a) The RMS of the residual wavefronts as a function of the number of subapertures with *SNRp* below 4. (b) The Strehl ratio of the corrected PSF as a function of the number of subapertures with *SNRp* below 4.

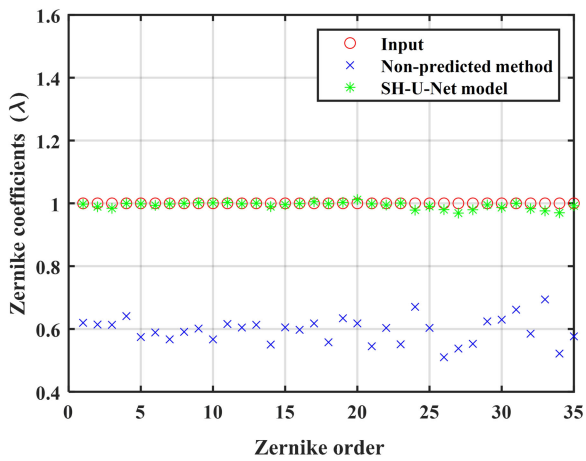

Fig. 10. Recovered first 35 Zernike mode coefficients with missing 40% of total sub-spots.

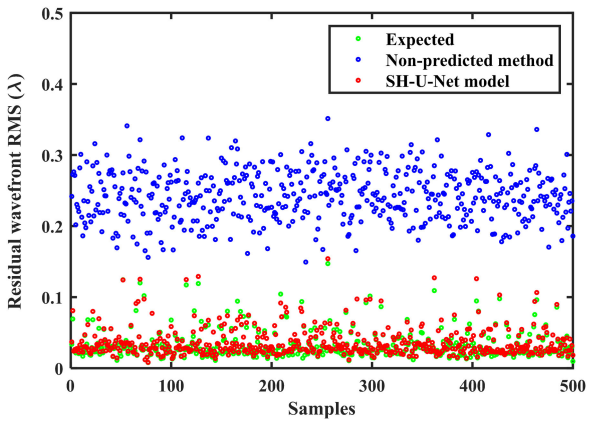

Fig. 11. The comparison of wavefront reconstruction errors.

To furth validate the wavefront detection performance of the proposed method, we randomly generated test sets containing 1500 sets data. The reconstruction results of 1500 test wavefronts are displayed in Fig. 9. Fig. 9(a) represent the RMS of the residual wavefronts as a function of the number of subapertures with *SNRp* below 4 for 1500 test data. The mean RMS of the residual wavefront for three methods are 0.2228λ (*TkCoG*), 0.1798λ (*TmCoG*), and 0.1401λ (SH-U-Net model), respectively. This suggests that our approach reduces the RMS of the residual wavefront by 37.12% (*TkCoG*) and 22.08% (*TmCoG*), respectively. Fig. 9(b) shows the SR of the corrected PSF as a function of the number of subapertures with *SNRp* below 4 for three methods. The mean SR of the corrected PSF are 0.3627, 0.4730, and 0.5749, respectively. The SR of this proposed method is about 1.59 and 1.22 times higher than that of the *TkCoG* and *TmCoG* approaches, respectively. These results suggest that the SH-U-Net model can help system to offer better compensation for wavefront aberrations and improve the Strehl ratio of the focal spot.

C. Validation on Data Outside the Training Set

In this subsection, we validate the generalizability and adaptability of the SH-U-Net model using wavefronts outside of the training set. We first evaluate the performance of the SH-U-Net model with single Zernike modes as incident wavefront. By taking the first 35 orders Zernike polynomial as an example,

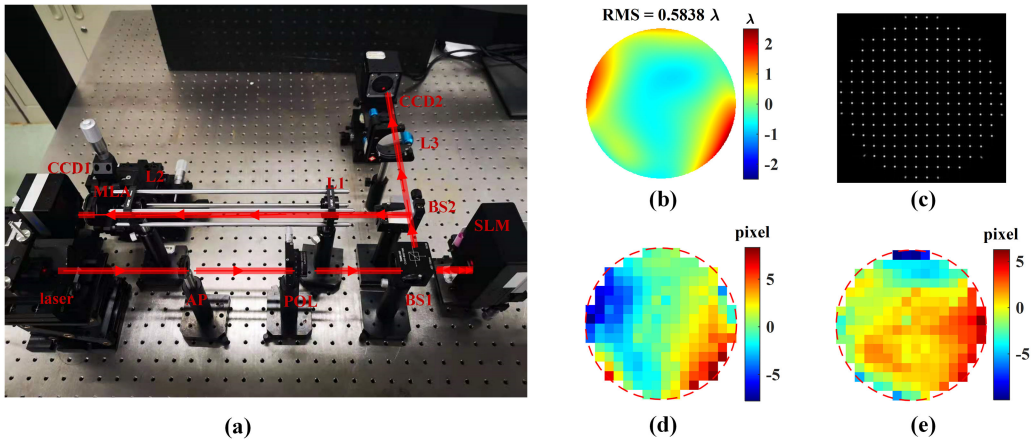

Fig. 12. (a) Experimental setup for the spot array pattern acquisition. (AP, aperture; POL, linear polarizer plate; BS1-BS2, non-polarizing beam splitter; SLM, spatial light modulator; L1-L3, relay lenses; MLA, microlens array; CCD1-CCD2; cameras.) (b) An aberration wavefront. (c) The output pattern of the SHWFS. (d) The *x* centroid displacements. (e) The *y* centroid displacements.

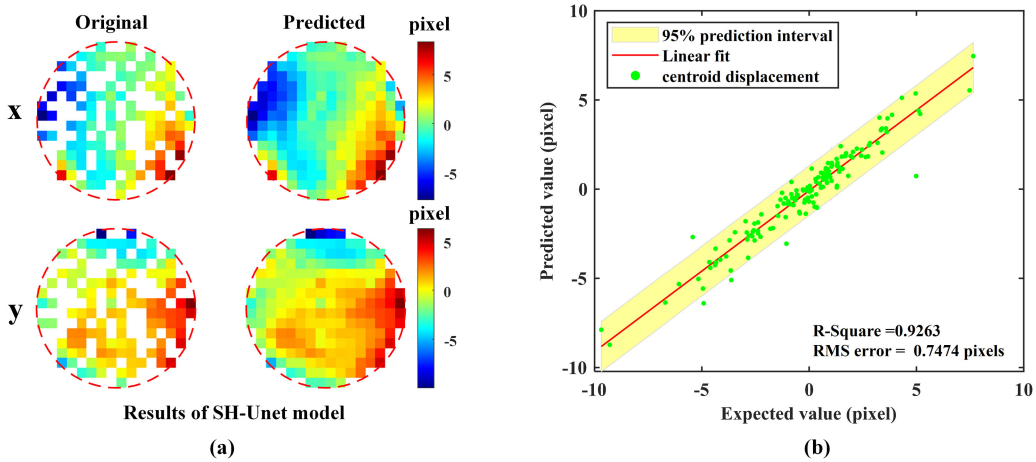

Fig. 13. Results of the SH-U-Net model prediction with missing 40% of total sub-spots. (a) The centroid displacements before and after prediction. (b) The Predicted centroid displacements versus the expected centroid displacements (ground truth).

TABLE III
THE ZERNIKE MODE COEFFICIENTS RANGES

Zernike order	Coefficients ranges / λ
1-5	-2.5~2.5
6-15	-1.5~1.5
16~35	-0.5~0.5

Fig. 10 analyzes the first 35 orders of Zernike coefficients recovered based on non-predicted and predicted methods when the single-order Zernike modes are used as the incident wavefront and the 40% of the total sub-spots in the output pattern of the SHWFS are missing randomly. It is evident that the reconstruction accuracy of the SHWFS is significantly improved with the help of the SH-U-Net model. The non-predicted method has a reconstruction accuracy of about 60% for single-order Zernike mode coefficients. By contrast, the SH-U-Net model's reconstruction accuracy nearly 100%.

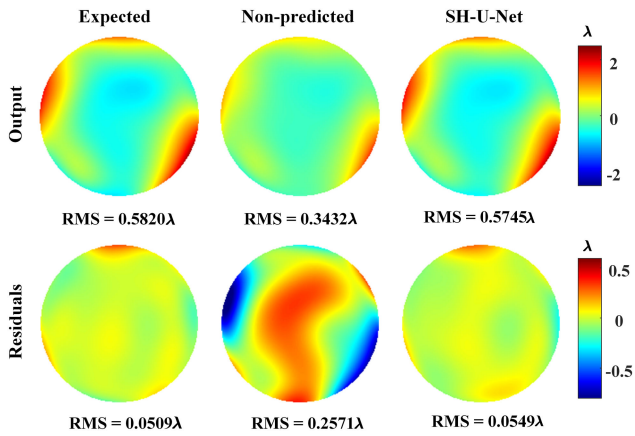

Fig. 14. The reconstructed wavefronts and residual wavefronts with missing 40% of total sub-spots.

To further validate the adaptability of the SH-U-Net model, 500 sets of incident wavefronts are randomly generated according to the coefficient ranges given in Table III. The percentage of sub-spots missing is set to 40%. But the locations of missing sub-spots are random. This means that each of the 500 spot image patterns has a different missing sub-spots location. The

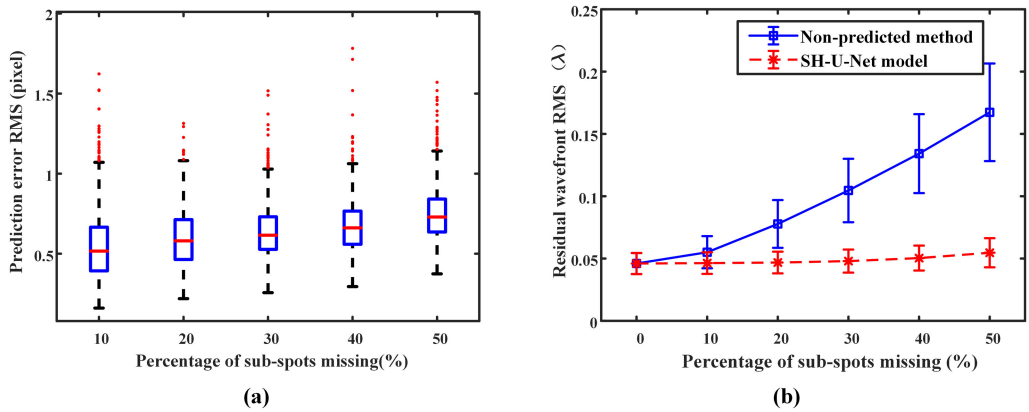

Fig. 15. The statistical results of the centroid displacement prediction and wavefront reconstruction for different scenarios. Each scenario contains 1000 datasets. (a) The RMS of centroid-displacement prediction errors. (b) The RMS of the residual wavefronts.

comparison of 500 wavefront reconstruction errors is shown in Fig. 11.

As expected, for such random wavefronts outside the training set, the SH-U-Net model is still able to predict the location of the missing spot. Compared with the residual wavefronts of the conventional method, the wavefront reconstruction errors of the SH-U-Net model are much close to that of the ideal scenario. This result indicates that the prediction of the SH-U-Net model does not need to know the locations of the missing sub-spots in advance and also works on wavefronts outside of the training group. The proposed method shows good generalization and adaptability.

IV. Experiment

An experiment is conducted to verify the validity of the proposed method. The setup is shown in Fig. 12(a). A collimated 635*nm* laser beam is the light source. The beam size is limited by an aperture (AP) with a diameter of 6.4*mm*. The linear polarizer (POL) is used to produce the polarized light needed for the liquid crystal on the silicon spatial light modulator (LCOS-SLM) which generates the distorted wavefront. The modulated beam is reflected by the beam splitter 1 (BS1) and divided into two beams by the beam splitter 2(BS2). One passes through an optical image transfer system consisting of L1 and L2 lenses into a 16×16 SHWFS (192 valid subapertures). The other one is focused on CCD2 by a lens (L3) as an auxiliary observation tool. The LCOS-SLM is located at the conjugate position of the entrance pupil plane of the SHWFS. Fig. 12(c) shows the output pattern of the SHWFS. Fig. 12(d) and (e) are the *x* and *y* centroid displacements, respectively. The parameters in the experiment are the same as those in Table I.

Firstly, we use the calibrated LCOS-SLM to generate 10000 random wavefronts (turbulence model parameter D/r_0 ranges from 5 to 10) and capture the corresponding output patterns of the SHWFS on the CCD. To obtain accurate centroid-displacement matrices, the centroids of the sub-spots are calculated through the *TmCoG* algorithm that can eliminate the effect of noise on the CCD. Then, the training samples are generated according to the method described in Section II.C. Finally, the SH-U-Net module is trained on the desktop workstation. The parameters and platform of the network training are the same as those of the simulation.

Fig. 13 shows the results predicted by the SH-U-Net model when 40% of total sub-spots are missing. Here, almost all of the predicted centroid displacements fall within the 95% confidence interval, indicating that the SH-U-Net model is able to predict the centroid displacements of the missing sub-spots accurately.

Wavefront is reconstructed based on the predicted centroid displacements and compared with the results without prediction. As shown in Fig. 14, the RMS of the residual wavefront is 0.0509λ in the ideal scenario (the expected scenario). With missing 40% of total sub-spots, the RMS of the residual wavefront of the non-predicted method rises to 0.2571λ and the incident wavefront cannot be reconstructed effectively. With the help of the SH-U-Net model, the centroid displacements of those missing sub-spots can be predicted precisely and then the incident wavefront can be reconstructed accurately. The RMS of the residual wavefront is reduced to 0.0549λ, which is pretty close to the ideal scenario.

Fig. 15 shows the statistical results of the centroid displacement prediction and wavefront reconstruction for different scenarios. Each scenario contains 1000 datasets. The results reveal the same trend as the simulation results. The average RMS of the residual wavefronts is 0.0460λ in the ideal scenario. Obviously, the RMS of the residual wavefronts of the non-predicted method is much higher than that of the ideal scenario, while the RMS of the residual wavefronts of the SH-U-Net model is close to the ideal scenario. When 40% of total sub-spots is missing, the average RMS of the residual wavefronts of the non-predicted method is 0.1342λ, which is almost twice as large as the ideal scenario. The average RMS of the residual wavefronts of the SH-U-Net model is 0.0504λ, which quite close to the ideal scenario.

V. Conclusion

Considering the effect of sub-spots missing on the wavefront reconstruction precision of the SHWFS, we propose a method of predicting undetected sub-spots' positions based on the information of detected sub-spots. With the designed SH-U-Net model, the information of missing sub-spots can be retrieved accurately,

which improves the measurement performance of the SHWFS. Numerical simulations are conducted to validate the feasibility and effectiveness of the proposed method. For wavefront measurement of weak light with non-uniform near-field intensity, our SH-U-Net model is able to achieve approximately 37.12% and 22.08% reduction in the RMS of the residual wavefront over the *TkCoG* and *TmCoG* approaches, respectively. The SR of the corrected PSF is about 1.59 and 1.22 times higher than that of the *TkCoG* and *TmCoG* approaches, respectively. Experimental results demonstrate that the proposed method can predict the sub-spots' centroid displacements accurately and reduce the RMS of the residual wavefront when some sub-spots are missing. In addition, the SH-U-Net model is evaluated by wavefronts outside of the training group and random miss sub-spots' locations, presenting its high adaptability and robustness in different scenarios. The method also reveals that partial accurate local slopes can be used to predict the complete slope distribution with the help of a deep neural network. However, the proposed method in the paper mainly deals with the missing information caused by the near-field non-uniformity of the beam and the limited dynamic range of the camera. In the next work, we will explore for the scenarios of absent information caused by discontinuous phase.

REFERENCES

[1] P. L. Wizinowich *et al.*, "The W. M. Keck observatory laser guide star adaptive optics system: Overview," *Publ. Astron. Soc. Pac.*, vol. 134, no. 840, pp. 297–309, Feb. 1965.

[2] N. Ji. "Adaptive optical fluorescence microscopy," *Nature Methods*, vol. 14, no. 4, pp. 374–380, Apr. 2017.

[3] M. J. Booth, "Adaptive optical microscopy: The ongoing quest for a perfect image," *Light: Sci. Appl.*, vol. 3, no. 4, pp. e165–e165, Apr. 2014.

[4] J. Liang, B. Grimm, S. Goelz, and J. F. Bille, "Objective measurement of wave aberrations of the human eye with the use of a Hartmann–Shack wave-front sensor," *J. Opt. Soc. Amer. A*, vol. 11, no. 7, pp. 1949–1957, Jul. 1994.

[5] A. Dubra *et al.*, "Noninvasive imaging of the human rod photoreceptor mosaic using a confocal adaptive optics scanning ophthalmoscope," *Biomed. Opt. Exp.*, vol. 2, no. 7, pp. 1864–1876, Jul. 2011.

[6] T. Li, L. Huang, and M. Gong, "Wavefront sensing for a nonuniform intensity laser beam by Shack–Hartmann sensor with modified fourier domain centroiding," *Opt. Eng.*, vol. 53, no. 4, Apr. 2014, Art. no. 044101.

[7] T. A. Planchon, J. P. Rousseau, F. Burgy, G. Chériaux, and J. P. Chambaret, "Adaptive wavefront correction on a 100-TW/10-Hz chirped pulse amplification laser and effect of residual wavefront on beam propagation," *Opt. Commun.*, vol. 252, no. 4, pp. 222–228, Aug. 2005.

[8] B. C. Platt and R. Shack, "History and principles of Shack-Hartmann wavefront sensing," *J. Refract. Surg.*, vol. 17, no. 5, pp. S573–S577, Sep. 2001.

[9] J. Y. Wang and D. E. Silva, "Wave-front interpretation with Zernike polynomials," *Appl. Opt.*, vol. 19, no. 9, pp. 1510–1518, May 1980.

[10] O. Soloviev and G. Vdovin, "Hartmann-Shack test with random masks for modal wavefront reconstruction," *Opt. Exp.*, vol. 13, no. 23, pp. 9570–9584, Nov. 2005.

[11] D. L. Fried, "Least-square fitting a wave-front distortion estimate to an array of phase-difference measurements," *J. Opt. Soc. Amer.*, vol. 67, no. 3, pp. 370–375, Mar. 1977.

[12] A. Talmi and E. N. Ribak, "Wavefront reconstruction from its gradients," *J. Opt. Soc. Amer. A*, vol. 23, no. 2, pp. 288–297, Feb. 2006.

[13] S. Thomas, T. Fusco, A. Tokovinin, M. Nicolle, V. Michau, and G. Rousset, "Comparison of centroid computation algorithms in a Shack–Hartmann sensor," *Mon. Not. R. Astron. Soc.*, vol. 371, no. 1, pp. 323–336, Apr. 2006.

[14] X. Li, X. Li, and C. Wang. "Optimum threshold selection method of centroid computation for Gaussian spot," in *Proc. SPIE 9675 AOPC* 2015*: Image Process. Anal.*, Beijing, China, 2015, Art. no. 967517.

[15] T. Sandrine, "Optimized centroid computing in a Shack-Hartmann sensor," in *Proc. SPIE 5490 Advancements Adaptive Optics Astronomical Telescopes + Instrumentation*, Glasgow, U.K., 2004, pp. 1238–1246.

[16] J. D. Barchers, D. L. Fried, and D. J. Link, "Evaluation of the performance of Hartmann sensors in strong scintillation," *Appl. Opt.*, vol. 41, no. 6, pp. 1012–1021, Feb. 2002.

[17] J. Notaras and C. Paterson, "Demonstration of closed-loop adaptive optics with a point-diffraction interferometer in strong scintillation with optical vortices," *Opt. Exp.*, vol. 15, no. 21, pp. 13745-13756, Oct. 2007.

[18] V. Akondi, S. Steven, and A. Dubra, "Centroid error due to non-uniform lenslet illumination in the Shack–Hartmann wavefront sensor," *Opt. Lett.*, vol. 44, no. 17, pp. 4167–4170, Sep. 2019.

[19] J. R. Crepp, S. O. Letchev, S. J. Potier, J. H. Follansbee, and N. T. Tusay, "Measuring phase errors in the presence of scintillation," *Opt. Exp.*, vol. 28, no. 25, pp. 37721–37733, Dec. 2020.

[20] D. Lechner, A. Zepp, M. Eichhorn, and S. Gładysz, "Adaptable Shack-Hartmann wavefront sensor with diffractive lenslet arrays to mitigate the effects of scintillation," *Opt. Exp.*, vol. 28, no. 34, pp. 36188–36205, Nov. 2020.

[21] C. Li, B. Li, and S. Zhang, "Phase retrieval using a modified Shack-Hartmann wavefront sensor with defocus," *Appl. Opt.*, vol. 53, no. 4, pp. 618–624, Feb. 2014.

[22] Z. Zhu *et al.*, "More Zernike modes' open-loop measurement in the sub-aperture of the Shack-Hartmann wavefront sensor," *Opt. Exp.*, vol. 24, no. 21, pp. 24611–24623, Oct. 2016.

[23] H. Guo, N. Korablinova, Q. Ren, and J. Bille, "Wavefront reconstruction with artificial neural networks," *Opt. Exp.*, vol. 14, no. 14, pp. 6456–6462, Jul. 2006.

[24] Z. Li and X. Li, "Centroid computation for Shack-Hartmann wavefront sensor in extreme situations based on artificial neural networks," *Opt. Exp.*, vol. 26, no. 24, pp. 31675–31692, Nov. 2018.

[25] L. Hu, S. Hu, W. Gong, and K. Si, "Learning-based Shack-Hartmann wavefront sensor for high-order aberration detection," *Opt. Exp.*, vol. 27, no. 23, pp. 33504–33517, Nov. 2019.

[26] R. Swanson, M. Lamb, C. Correia, S. Sivanandam, and K. Kutulakos, "Wavefront reconstruction and prediction with convolutional neural networks," in *Proc. SPIE 10703, Adaptive Opt. Syst. VI Astronomical Telescopes + Instrumentation*, Austin, Texas, USA, 2018, pp. 481–490.

[27] T. B. DuBose, D. F. Gardner, and A. T. Watnik, "Intensity-enhanced deep network wavefront reconstruction in Shack–Hartmann sensors," *Opt. Lett.*, vol. 45, no. 7, pp. 1699–1702, Apr. 2020.

[28] L. Hu, S. Hu, W. Gong, and K. Si, "Deep learning assisted Shack–Hartmann wavefront sensor for direct wavefront detection," *Opt. Lett.*, vol. 45, no. 13, pp. 3741–3744, Jul. 2020.

[29] A. Polo, V. Kutchoukov, F. Bociort, S. F. Pereira, and H. P. Urbach, "Determination of wavefront structure for a hartmann wavefront sensor using a phase-retrieval method," *Opt. Exp.*, vol. 20, no. 7, pp. 7822–7832, Mar. 2012.

[30] X. Y. Ma, C. H. Rao, and H. Q. Zheng, "Error analysis of CCD-based point source centroid computation under the background light," *Opt. Exp.*, vol. 17, no. 10, pp. 8525–8541, May 2009.

[31] O. Ronneberger, P. Fischer, and T. Brox, "U-Net: Convolutional networks for biomedical image segmentation," in *Proc. MICCAI*, 2015, pp. 234–241.

[32] R. J. Noll, "Phase estimates from slope-type wave-front sensors," *J. Opt. Soc. Am.*, vol. 68, no. 1, pp. 139–140, Jan. 1978.

[33] Y. He, Z. Liu, Y. Ning, J. Li, X. Xu, and Z. Jiang, "Deep learning wavefront sensing method for shack-hartmann sensors with sparse sub-apertures," *Opt. Exp.*, vol. 29, no. 11, pp. 17669–17682, May 2021.

[34] M. J. Steinbock, M. W. Hyde, and J. D. Schmidt, "LSPV+7, a branch-point-tolerant reconstructor for strong turbulence adaptive optics," *Appl. Opt.*, vol. 53, no. 18, pp. 3821–3831, Jun. 2014.